Deactivation of Sn-Beta Zeolites Caused by Structural Transformation of Hydrophobic to Hydrophilic Micropores during Aqueous-Phase Glucose Isomerization

Journal:	*Catalysis Science & Technology*
Manuscript ID	CY-ART-12-2018-002589.R1
Article Type:	Paper
Date Submitted by the Author:	28-Feb-2019
Complete List of Authors:	Cordon, Michael; Purdue University, Davidson School of Chemical Engineering Hall, Jacklyn; Purdue University, Davidson School of Chemical Engineering Harris, James; Purdue University, Davidson School of Chemical Engineering Bates, Jason; Purdue University, Davidson School of Chemical Engineering Hwang, Sonjong; California Institute of Technology, Chemistry and Chemical Engineering Gounder, Rajamani; Purdue University, Davidson School of Chemical Engineering

Journal Name

ARTICLE

Deactivation of Sn-Beta Zeolites Caused by Structural Transformation of Hydrophobic to Hydrophilic Micropores during Aqueous-Phase Glucose Isomerization

Received 00th January 20xx,
Accepted 00th January 20xx

DOI: 10.1039/x0xx00000x

www.rsc.org/

Michael J. Cordon[a], Jacklyn N. Hall[a], James W. Harris[a], Jason S. Bates[a], Son-Jong Hwang[b], Rajamani Gounder[1,*]

The structural changes underlying the deactivation of Sn-Beta zeolites under aqueous-phase reaction conditions at elevated temperatures (373 K) are investigated using spectroscopic characterization and site titration techniques together with turnover rates for glucose isomerization, a well-understood probe reaction for which changes in measured rates can be ascribed to specific changes in catalyst structure. In the case of hydrophobic, low-defect Sn-Beta zeolites (Sn-Beta-F), treatment in hot liquid water (373 K) for short times (<1 h) prior to reaction causes glucose-fructose isomerization turnover rates (per open Sn site, 373 K) to increase, while longer-term exposure (>3 h) to hot liquid water causes turnover rates to decrease and approach values characteristic of hydrophilic, defect-rich Sn-Beta zeolites (Sn-Beta-OH). In contrast, turnover rates on hydrophilic Sn-Beta-OH zeolites are insensitive to the duration of hot liquid water exposure prior to reaction. Activation and deactivation phenomena on Sn-Beta-F zeolites occur concomitantly with the formation of silanol defects (by ~2–10x) with increasing durations (0–24 h) of hot water treatment, despite negligible differences in open and closed Sn site speciation as quantified ex situ by CD_3CN IR spectra. Mechanistic interpretations of these phenomena suggest that silanol groups present at low densities serve as binding sites for water molecules and clusters, which confer enthalpic stability to kinetically-relevant hydride-shift transition states and increase turnover rates, while silanol groups present in higher densities stabilize extended hydrogen-bonded water networks, which entropically destabilize kinetically-relevant transition states and decrease turnover rates. Intraporous voids within hydrophobic Sn-Beta-F zeolites become increasingly hydrophilic as silanol groups are formed by hydrolysis of framework siloxane bridges with increasing durations of water treatment, thereby decreasing aqueous-phase glucose isomerization turnover rates (per open Sn site). These findings suggest design strategies that suppress framework hydrolysis would attenuate the deactivation of Lewis acid zeolites in aqueous media.

1. Introduction

Lewis acidic molecular sieves are silica-based microporous materials with some of their framework silicon atoms isomorphously substituted with tetravalent heteroatoms (M^{4+} = Sn^{4+}, Ti^{4+}, etc.), which are useful catalysts for alkene epoxidation[1, 2] and transformations of biomass-derived oxygenates[3]. Active sites in these materials comprise both Lewis acidic binding sites, present because of differences in electronegativity between lattice M^{4+} and Si^{4+} centers, and their confining environments[4], which vary in size and polarity among materials of different framework topology and synthetic and treatment history. Active sites within inorganic Lewis acidic molecular sieves catalyze glucose isomerization by an analogous reaction mechanism to that reported for metalloenzymes (e.g., D-xylose isomerase)[5], but are more tolerant to variations in solvent pH, temperature, and impurity concentrations than are immobilized metalloenzymes[6]. One challenge to practical implementation of Lewis acidic molecular sieves, however, is the deactivation typically observed under aqueous-phase conditions[4, 7-9].

Mechanistic understanding of such deactivation phenomena has been limited by the complexity of *in situ* quantification of the interactions between liquids and solids[4], although recent research has provided insights on the nature of zeolite degradation in liquid water. Al-Beta zeolites deactivate significantly when treated in hot liquid water (48 h, 433–573 K) because intraporous water facilitates the hydrolysis of framework siloxane bonds and amorphization of crystallites[10-12]. Silanol defects stabilize water molecules, clusters of water molecules and extended hydrogen-bonded networks of water molecules between hydrophobic SiO_2 plates positioned 0.7 nm apart in molecular dynamics simulations

[a] Charles D. Davidson School of Chemical Engineering, Purdue University, 480 Stadium Mall Drive, West Lafayette, IN 47907, USA
[b] Division of Chemistry and Chemical Engineering, California Institute of Technology, Pasadena, CA 91101, USA
* Corresponding author. E-mail: rgounder@purdue.edu
Electronic Supplementary Information (ESI) available. See DOI: 10.1039/x0xx00000x

(300 K)[13], and these silanol defects decrease zeolite stability during gas-phase water exposure (473 K, 0–24 h) as observed using X-ray diffraction (XRD) to assess crystallinity and diffuse reflectance IR spectroscopy (DRIFTS) to monitor silanol group formation[14]. This amorphization can be suppressed via functionalization of external zeolite surfaces with hydrophobic organosilanes, which hinders direct contact between zeolite crystallites and the aqueous phase[14-16] and, in turn, the solvation of intraporous fragments formed upon zeolite framework hydrolysis and their transport to bulk solvent phases[17]. Higher intraporous water densities also accelerate catalyst deactivation and decrease reaction rates for coupled transfer hydrogenation and etherification of 5-hydromethylfurfural in primary and secondary alcohols on Zr-Beta, Hf-Beta, and Sn-Beta zeolites[7], dihydroxyacetone isomerization in methanol on Sn-Beta, Sn-MOR, and Sn-FAU zeolites[8], aqueous-phase cyclohexanol dehydration on Al-Beta zeolites[10], and liquid-phase glucose-fructose isomerization on Sn-Beta zeolites in both water and methanol[18, 19]. These observations are consistent with higher glucose isomerization rates reported on Sn-Beta zeolites when samples are dehydrated before exposure to aqueous reactant solutions[20].

Glucose-fructose isomerization is an aqueous-phase probe reaction for which the reaction mechanism and active sites are commonly accepted, as it is catalyzed over partially-hydrolyzed Lewis acidic open Sn sites ($Sn(OSi)_3OH$) on Sn-Beta zeolites[21-23], involves kinetically-relevant intramolecular 1,2-hydride shift[24] with negligible formation of undesired side products at initial reaction times[24-26], and is sensitive to confining environment polarity[22, 27]. Glucose isomerization over Sn-Beta catalysts proceeds by quasi-equilibrated adsorption of glucose from solution onto the Lewis acid site, followed by quasi-equilibrated ring-opening and deprotonation, and then by kinetically-relevant 1,2-hydride shift to form ring-opened fructose[21]. The 1,2-hydride shift transition state has been detected by isotopically labeling the glucose C_2-H with D and monitoring the retained D label in fructose products in the C_1-D position via ^{1}H NMR[24]. The involvement of this 1,2-hydride shift transition state in the sole kinetically relevant step has been verified through measurement of the glucose-H2/D2 kinetic isotope effect (KIE) of 2.1 at 373 K[21], and from quantum mechanics/molecular mechanics (QM/MM) calculations on M^{4+}-Beta and M^{5+}-Beta zeolites[28]. Furthermore, this KIE value of 2.1 (at 373 K) indicates that rate data are uncorrupted by mass transfer artifacts, which in the limit of severe intracrystalline transport restrictions would result in measurement of the square root of the theoretical KIE value (1.4 at 373 K)[27]. Initial rate measurements on Sn-Beta zeolites are first-order in initial glucose concentration (1-10 wt%, 373 K)[22] and reflect free energy differences between 1,2-hydride shift transition states and two water molecules bound to open Sn sites, a reference state that has been observed in diffuse-reflectance UV-Visible spectra[22, 29, 30], ^{119}Sn NMR spectra[26, 31, 32], and X-ray absorption spectra[33-35]. Further, free energy differences reflected in aqueous-phase glucose isomerization rates are sensitive to intraporous silanol defect density, because silanol groups stabilize co-adsorbed hydrogen bonding networks of water molecules that increase free energy barriers[36] and lead to lower initial isomerization rates on Ti-Beta and Sn-Beta[22, 29].

Here, we investigate systematic changes to Sn site densities and the polarity of microporous confining environments on Sn-Beta zeolites after extended durations (0–24 h) of hot water exposure at 373 K. Aqueous-phase glucose isomerization rates measured in batch reactors, after Sn-Beta zeolites were exposed to hot liquid water for increasing times, are used to simulate the deactivation behavior reported previously during continuous aqueous-flow rate measurements[8, 19, 37]. IR spectra collected after CD_3CN titration of framework and extraframework Sn sites and silanol defect groups, combined with single-component vapor-phase water and methanol adsorption isotherms and ^{29}Si and ^{19}F solid-state NMR spectra, were used to monitor and quantify changes in the densities of surface functional groups caused by hot water exposure. These changes in surface species are correlated with observed deactivation and activation phenomena to isolate the role of silanol defects, and the co-adsorbed water molecules and extended hydrogen bonding networks they stabilize during reaction, on changes to the stability and catalytic reactivity of Sn-Beta zeolites under aqueous-phase reaction conditions.

2. Experimental Methods

2.1. Catalyst Synthesis and Preparation

Sn-Beta zeolites were synthesized in fluoride media (Sn-Beta-F) using previously reported methods[22, 29, 38]. Dealuminated Beta zeolites were used as seed material and were prepared by stirring a mixture of 5 g of H-form Al-Beta (Zeolyst, CP814C, Si/Al = 19) and 125 cm^3 of concentrated nitric acid (HNO_3, Avantor, 69 wt%) for 16 h at 353 K. Solids were then collected through centrifugation, washed in deionized water (18.2 MΩ, 6 washes, 25 cm^3 (g zeolite)$^{-1}$ per wash), and dried at 373 K for 16 h. Preparation of the synthesis gels used to crystallize Sn-Beta-F samples involved mixing 7.67 g of tetraethylammonium hydroxide (TEAOH, Sachem, 35 wt%) with 6.98 g of tetraethylorthosilicate (TEOS, Sigma Aldrich, >98 wt%) in a perfluoroalkoxy (PFA) alkane (Savillex Corp.) container and then stirring for 1 h. Then, a solution containing 0.04–0.12 g of tin (IV) chloride pentahydrate ($SnCl_4{\cdot}5H_2O$, Sigma-Aldrich, 98 wt%) dissolved in 0.64 g of deionized water was added to the gel prior to sealing the PFA container and stirring for 12 h. The cap was then removed to allow for the evaporation of ethanol and excess water. Then, 0.74 g of hydrofluoric acid (HF, Alfa Aesar, 48%) were added to the solution and stirred manually for 300 s. The resulting gel was loaded into a Teflon-lined stainless steel autoclave (45 cm^3, Parr Instruments) and 0.085 g of dealuminated Beta zeolite seeds were added. The autoclave was then sealed and placed in an isothermal oven (Yamato DKN-402C) at 413 K for 6–25 d while rotating at 60 RPM. The autoclaves were then cooled to ambient temperature and the resulting solids were washed thoroughly with water and acetone (Sigma Aldrich, >99.5 wt%,

5 washes per solvent, 25 cm^3 (g zeolite)$^{-1}$ per wash), separated by centrifugation, and then dried for 16 h at 373 K. The dry powders were heated in dry air (Ultra Zero Grade, Indiana Oxygen, 1.67 cm^3 s^{-1}(g zeolite)$^{-1}$) to 853 K (0.0167 K s^{-1}) and held for 10 h in a muffle furnace (Nabertherm LE 6/11 equipped with a P300 controller). Samples are labeled as Sn-Beta-F-X, where X is the Si/Sn ratio determined from atomic absorption spectroscopy (AAS). Some of these samples (Sn-Beta-F-100, Sn-Beta-F-220, Sn-Beta-F-172, and Sn-Beta-F-110) have been studied in our prior publications[22].

Post-synthetic Sn-Beta-OH zeolite samples were synthesized via $SnCl_4$ grafting as reported previously in dichloromethane reflux[29]. Briefly, Al-Beta-OH samples were synthesized hydrothermally using previously reported procedures[38] (Si/Al = 29–55). Subsequently, the Al-Beta-OH parent materials were dealuminated by stirring in nitric acid (Avantor, 25 cm^3 (g Al-Beta-OH zeolite)$^{-1}$, 69 wt%) at 353 K overnight. The dealuminated Beta obtained was washed thoroughly with water and dried at 373 K overnight in a drying oven. Next, the dealuminated Beta was loaded into a 500 cm^3 three-neck round-bottom flask with a septum stopper (white rubber, Ace Glass) and connected to a Schlenk line prior to drying under rough vacuum (~0.04 Torr, Oerlikon Trivac 140002E2) at 423 K overnight. Dichloromethane (DCM, Sigma Aldrich, 99.8%) was dried separately in an inert atmosphere (Ar, Indiana Oxygen, 99.999%) over pre-activated molecular sieves (W. R. Grace, Type 3AA, Grade 562, 4–8 mesh) in a separate round bottom flask for 72 h, then transferred via air-free and moisture-free cannula to the round-bottom flask containing the dried dealuminated Beta. Finally, 1 M $SnCl_4$ in DCM (Sigma Aldrich, 0.001–0.040 mol Sn (g zeolite)$^{-1}$) was transferred via moisture-free cannula to the round-bottom flask containing the dealuminated Beta and DCM, and the mixture was stirred under reflux conditions (333 K) in Ar atmosphere for 7 h. The resulting solids were separated by centrifugation and thoroughly washed with methanol (99.9%, Sigma Aldrich, ~120 cm^3 (g zeolite)$^{-1}$) to reduce the formation of extraframework Sn oxide[39]. Solids were then dried overnight at 373 K prior to treatments in air (1.67 cm^3 s^{-1} (g zeolite)$^{-1}$) at 473 K (0.05 K s^{-1}) for 6 h and then at 823 K (0.05 K s^{-1}) for 6 h in a muffle furnace. Samples prepared post-synthetically are subsequently labeled as Sn-Beta-OH-X, where X is the Si/Sn ratio determined from AAS.

Hot (373 K) water treatment of Sn-Beta catalysts were performed by loading ~0.3 g of catalyst evenly among three 10 cm^3 thick-walled glass batch reactors (VWR) and adding water adjusted to pH 4 with hydrochloric acid (HCl, Macron, 37 wt%) to each reactor to achieve a 1:50 catalyst to water ratio, which is the same pH and catalyst to solution ratio used in glucose isomerization kinetic studies. The reactors were heated to 373 K and stirred at 750 RPM for variable exposure times (0.08–24 h). After the specified time, the reactors were quenched in an ice bath and the water-treated solids were collected via centrifugation, and then dried overnight in an oven (363 K).

2.2. Catalyst Characterization

Elemental compositions of catalyst samples were determined by atomic absorption spectroscopy (AAS) using a Perkin Elmer AAnalyst 300 Atomic Absorption Spectrometer. Calibration standards for each metal tested were created from 1000 ppm AAS standards (Alfa Aesar, TraceCERT, ±4 ppm). Samples were prepared for AAS analyses by dissolving ~0.02 g solid in 2.6 g of HF (48 wt%, Alfa Aesar) overnight prior to the addition of 50 g of deionized water. Absorbance values were measured at 396.2 nm and 284.0 nm in an acetylene/nitrous oxide flame for Al and Sn, respectively. Si/Al and Si/Sn ratios were determined from the Al and Sn weight fractions obtained by AAS together with the unit cell formula for zeolite Beta.

Powder X-ray diffraction (XRD) patterns were obtained using a Rigaku Smartlab X-ray diffractometer equipped with an ASC-6 automated sample changer and a Cu Kα X-ray source (1.76 kW). Approximately 0.01 g of sample were loaded into low dead volume, zero background sample holders (Rigaku) prior to diffraction pattern collection (4-40°, can rate of 0.00417° s^{-1}, step size of 0.01°). The presence of large (>3 nm) SnO_x domains, reflected by peaks located at 26.7 and 34°, were not observed in XRD patterns.

Scanning electron microcopy (SEM) images were obtained using a FEI Quanta 3D FEG Dual-beam SEM with an Everhart-Thornley attachment for high vacuum imaging. The focused beam operating mode was used (5 kV, spot size of 4 μm) to collect SEM micrographs.

Gas-phase nitrogen (77 K), and vapor-phase water (293 K) and methanol (293 K) adsorption isotherms were measured with a Micrometrics ASAP2020 Surface Area and Porosity Analyzer. ~0.03 g of catalyst were pelleted and sieved to 180–250 μm and loaded for analysis. Sample degas was performed by heating samples to 623 K (0.0167 K s^{-1}) under vacuum (<0.005 Torr) for 8 h prior to adsorption measurements. Micropore volumes were determined from a semi-log derivative analysis of nitrogen adsorption isotherms. Water uptakes at a reduced pressure of 0.2 were reported for comparison between samples, and a reduced pressure of 0.2 is a reference pressure associated with completion of micropore filling by cyclohexane (298 K) within hydrophobic zeolites[40].

Diffuse reflectance UV-visible spectroscopy was performed using a Varian Cary 5000 spectrometer with a Harrick Praying Mantis *in situ* diffuse reflectance cell. Spectra were collected after heating the sample to 523 K (~0.5 K s^{-1}) under dry He flow (4.17 cm^3 s^{-1} (g zeolite)$^{-1}$) and holding the sample at 523 K for 0.5 h. Polytetrafluoroethylene (PTFE, 1 μm, Sigma Aldrich) was used as the baseline, 100% reflectance standard. Spectra were processed using the Kubelka-Munk function (F(R)).

Infrared spectroscopy experiments were performed in a custom-built IR cell and heating/cooling chamber[41] by first pressing self-supporting wafers of Sn-Beta zeolite samples prior to placing them in a custom quartz cell placed in an insulated brass block. The quartz cell was sealed with custom ultra-torr fittings equipped with CaF_2 windows. The IR cell was connected to a custom glass manifold and the wafer was treated in flowing air (Parker Balston, <1 ppm CO_2, 200 K H_2O dew point) at 823 K (0.0833 K s^{-1}) for 1 h. The wafer was then exposed to vacuum (~10^{-2} Torr) for 1 h at 823 K then cooled to

303 K. Infrared spectra (64 scans, 2 cm^{-1} resolution) were collected using a Nicolet 4700 spectrometer equipped with a HgCdTe detector cooled with liquid nitrogen (77 K). A spectrum was collected prior to deuterated acetonitrile (CD_3CN) dosing and was subtracted from spectra collected after each dose. Known quantities of CD_3CN (~1.5 x 10^{-7} mol) were prepared in a calibrated volume, dosed into the cell, and allowed to equilibrate for 180 s. Dosing was repeated until saturation as determined from significant pressures (>0.4 Torr) remaining after equilibration, indicating residual CD_3CN vapor. Spectra collected on samples treated in hot (373 K) liquid water were collected in a similar fashion except that the samples were heated to 673 K (0.0833 K s^{-1}) in dry He flow prior to vacuum exposure (1 h) and cooling to 303 K for dosing.

Infrared spectra were deconvoluted in CasaXPS using a previously reported procedure and integrated peak areas for peaks centered at 2316 cm^{-1}, 2308 cm^{-1}, 2287 cm^{-1}, and 2275 cm^{-1} were quantified[22]. Integrated molar extinction coefficients (E) for each peak were previously reported and were used to convert integrated peak areas into total densities of open and closed Lewis acidic Sn sites, extraframework Sn sites, and silanol groups, respectively[42].

Solid-state magic angle spinning (MAS) and cross-polarization MAS (CPMAS) NMR spectra were collected using a Bruker Avance 500 MHz spectrometer equipped with a Bruker 4 mm MAS probe. ~75 mg of Sn-Beta was packed into a 4 mm ZrO_2 rotor. The operating frequencies were 99.5 and 470.5 MHz for ^{29}Si and ^{19}F nuclei, respectively. Spectra were externally referenced to tetramethylsilane (TMS) for ^{29}Si and $CFCl_3$ for ^{19}F. For ^{29}Si CPMAS spectra, contact pulse of 62.5 kHz radio-frequency (rf) pulse power was applied while ^{1}H contact rf power was adjusted at 54.5 kHz at sample spinning rate of 8 kHz for optimal CPMAS condition. ^{19}F MAS spectra were recorded under 14 kHz of sample spinning and without ^{1}H decoupling pulse.

2.3. Glucose Isomerization Kinetic Studies

Kinetic studies were performed with 1–2 wt% aqueous D-glucose (Sigma-Aldrich, ≥99.5%) solutions in 10 cm^3 thick-walled glass batch reactors (VWR). Reactant solutions were prepared by first lowering the pH of deionized water to 4 with hydrochloric acid to suppress background glucose isomerization reactivity from hydroxide anions in solution prior to dissolving D-glucose in the pH-adjusted water to obtain the desired concentration. Reactant solutions were then filtered (0.2 μm PTFE filters, VWR) and loaded into 2 cm^3 glass vials capped with a PTFE/silicone septum for pre-heating to reaction temperature. Typically ~0.01 g of catalyst were added to the batch reactor and sealed in with a crimp top (PTFE/silicone septum, Aligent). Batch reactors and vials containing reactant solutions were heated separately for 600 s to 373 K in an oil bath atop a digital stirred hotplate (IKA RCT basic). Reactions were initiated by injecting ~1 cm^3 of the pre-heated reactant solution into the capped batch reactor. Reactors were held at temperature (373 K, 750 RPM, autogeneous pressure) for various reaction times (0.08–1 h) to ensure differential conversions (<6%). Under these conditions, measured reaction rates are equivalent to initial rate measurements obtained from batch reactor kinetic studies, in which aliquots are taken at multiple time points, and measured fructose concentrations are regressed to a reversible batch reactor model in order to extract initial fructose formation rates.

After reaction, batch reactors were quenched in an ice bath and product solutions were collected and filtered through 0.2 μm PTFE filters (VWR). Product solutions were mixed with a 1 wt% aqueous D-mannitol (Sigma Aldrich, ≥98 wt%) solution as an internal standard for product quantification. A high-performance liquid chromatograph (HPLC, Agilent 1260) equipped with a Hi-Plex Ca column (7.7 x 300 mm, 8 μm particle size, Agilent) and an aqueous mobile phase (0.01 cm^3 s^{-1}, 353 K) was used to separate isomerization products. Quantification was performed using an evaporative light scattering detecter (Agilent 1260 Infinity ELSD) and individual calibration curves for reactant and product compounds.

To collect reaction rates after extended durations of water exposure, ~0.01 g of catalyst were loaded into a batch reactor followed by the addition of ~0.5 cm^3 of pH-adjusted water, achieving an approximate 1:50 catalyst to water mass ratio. The reactor was then capped with a crimp top and heated (373 K, 750 RPM) in an oil bath for 0.08-24 h. After the desired water exposure time, the reaction was initiated by the injection of ~0.5 cm^3 of a 2 wt% aqueous glucose solution (heated to 373 K for 600 s prior to injection) to produce a bulk glucose concentration of ~1 wt% in the reactant solution. Reaction times were chosen (0.08–1 h) to maintain differential conversions (<6%). Products were subsequently quantified as described above. Glucose-fructose isomerization rate constants measured on Sn-Beta-F samples immediately after extended water exposure, and those measured on Sn-Beta-F samples dried after hot water exposure prior to the onset of reaction (as performed on untreated Sn-Beta samples), were identical within experimental error.

3. Results and Discussion

3.1. Effect of Hot Water Pretreatment of Sn-Beta on Glucose Isomerization Kinetics.

Sn-Beta zeolites were synthesized hydrothermally in fluoride media or using post-synthetic methods to graft $SnCl_4$ precursors within vacancy defects of dealuminated Beta frameworks in order to obtain hydrophobic Sn-Beta-F and hydrophilic Sn-Beta-OH samples, respectively. Powder X-ray diffraction patterns (Figure S.1, Supp. Info.) and micropore volumes (Table 1) derived from N_2 adsorption isotherms (77 K, Figure S.2, Supp. Info.) of all Sn-Beta samples were consistent with the Beta topology. Higher signal-to-noise ratios in XRD patterns measured for Sn-Beta-F samples reflect larger crystallite sizes than Sn-Beta-OH samples, as previously noted for Sn-Beta[22] and Ti-Beta[36]. Absorption edge energies, estimated from Tauc plots of diffuse reflectance UV-Visible spectra measured after dehydration of Sn-Beta-F and Sn-Beta-

OH samples (523 K, Figures S.3 and S.4, Supp. Info.), are listed in Table 1 and are characteristic of isolated Sn^{4+} centers within zeolite frameworks (≥4.1 eV) on all samples[43]. The number of open Sn sites, closed Sn sites, and silanol groups (per g) are also listed in Table 1, as quantified from IR peak areas measured on Sn-Beta samples titrated with CD_3CN to saturation coverages (Figure S.5, Supp. Info.) and previously reported integrated molar extinction coefficients (E(2316 cm^{-1}) = 1.04 ± 0.22 cm μmol^{-1}, E(2308 cm^{-1}) = 2.04 ± 0.43 cm μmol^{-1}, E(2275 cm^{-1}) = 0.74 ± 0.16 cm μmol^{-1}, respectively)[22]. Vapor-phase water adsorption isotherms (293 K, Figure S.6, Supp. Info.), water uptakes quantified at P/P_0 = 0.2 (Table 1), and methanol adsorption isotherms (293 K, Figure S.7, Supp. Info.) on all Sn-Beta-F and

Table 1. Characterization data on Sn-Beta-F and Sn-Beta-OH zeolites.

Sample	V_{ads} (N_2, 77 K) ($cm^3\ g^{-1}$)[a]	Edge Energy (eV)[b]	Open Sn Density (10^5 mol $Sn_{LA}\ g^{-1}$)[c]	Closed Sn Density (10^5 mol $Sn_{LA}\ g^{-1}$)[c]	Silanol Density (10^5 mol $Sn_{LA}\ g^{-1}$)[c]	V_{ads} (H_2O, 293 K) ($10^3\ cm^3\ g^{-1}$, P/P_0=0.2)[d]
Sn-Beta-F-100	0.24	4.1	2.09	5.97	5.88	6.9
Sn-Beta-F-172	0.21	4.2	1.86	6.36	9.81	7.3
Sn-Beta-F-220	0.22	4.3	2.48	4.44	10.30	5.0
Sn-Beta-F-116	0.23	4.3	5.09	9.11	12.29	10.5
Sn-Beta-F-110	0.23	4.3	5.14	9.83	9.30	9.5
Sn-Beta-OH-80	0.24	5.5	8.48	11.92	90.90	84.4
Sn-Beta-OH-94	0.17	5.5	10.79	9.07	14.50	23.4
Sn-Beta-OH-84	0.22	5.5	4.62	18.69	73.70	94.6

[a] N_2 volumes at the end of micropore filling transition (77 K).

[b] Determined from Tauc plots after dehydration (523 K).

[c] Lewis acidic Sn densities and silanol densities measured from CD_3CN titration IR experiments.

[d] Water uptake at P/P_0=0.2 (293 K).

Sn-Beta-OH samples[40] are consistent with previously reported data for hydrophobic and hydrophilic Beta zeolites[22]. Taken together, the bulk properties of all Sn-Beta-F and Sn-Beta-OH samples studied here are characteristic of the hydrophobic and hydrophilic Sn-Beta samples reported in our prior work[22, 29, 44].

Figure 1A shows measured first-order glucose-fructose isomerization rate constants for Sn-Beta-F-116, normalized by the number of open Sn sites quantified *ex situ* (Table 1), as a function of hot (373 K) water exposure time before the onset of reaction. First-order rate constants are higher (by ~2x) on samples exposed to water for short exposure times (0–1 h, Figure 1A), but decrease monotonically with increasing water exposure time (6–24 h) and eventually become lower than rate constants measured on untreated samples. First-order isomerization rate constants on Sn-Beta-F-116 are measured from initial reaction time data; therefore, differences in such rate constants reflect activation phenomena that occur at short water exposure times and deactivation phenomena that occur at longer water exposure times, but prior to glucose isomerization catalysis in both cases. Similar activation phenomena have been observed for glucose-fructose isomerization on Sn-Beta catalysts in methanol solvent in initial time-on-stream measurements (0–36 h, 383 K under continuous flow conditions)[18, 19].

Several additional hydrophobic Sn-Beta-F and hydrophilic Sn-Beta-OH samples of varying Sn content (Si/Sn = 80–220) were studied in an analogous manner to that used for Sn-Beta-F-116 in order to probe whether analogous activation and deactivation phenomena were observed generally on samples of varying composition and synthetic provenance. Figure 1B shows measured first-order glucose isomerization rate constants for five hydrophobic Sn-Beta-F samples and three hydrophilic Sn-Beta-OH samples, normalized by the number of open Sn sites quantified *ex situ* on samples prior to hot water treatment (Table 1), as a function of water exposure time (373 K). Previously reported first-order rate constants vary (by 3x at 373 K, per Sn) among Sn-Beta-F samples (Si/Sn = 100–220)[22], and decrease systematically with increasing Sn content among Sn-Beta-OH samples prepared by post-synthetic grafting of Sn into a dealuminated Beta support[29]. Rates are similar (within ~3x) for Sn-Beta-F and for Sn-Beta-OH samples when normalized by the number of open Sn sites, and those for Sn-Beta-OH samples no longer depend systematically on Sn content[22]. Among the Sn-Beta-F and the Sn-Beta-OH samples studied here (four of which belong to a larger suite of samples we have studied previously[22]), first-order rate constants (373 K, per open Sn) vary within this factor of ~3x, which is reasonable agreement considering that there may be residual

Journal Name

ARTICLE

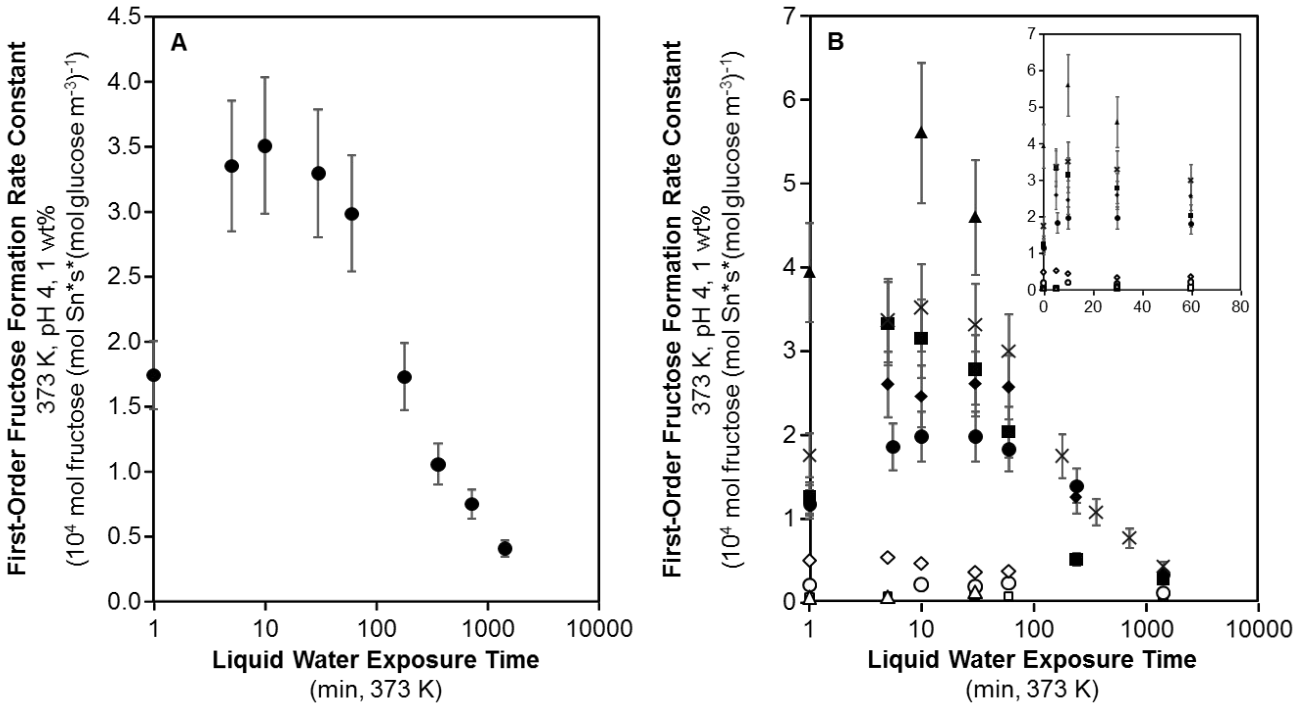

Figure 1. A) Measured first-order glucose isomerization rates (per open Sn, 373 K) on Sn-Beta-F-116 after liquid water exposure for various durations (0-24 h, 373 K). B) Measured first-order glucose isomerization rates (per open Sn, 373 K) on Sn-Beta-F-100 (■), Sn-Beta-F-110 (▲), Sn-Beta-F-116 (X), Sn-Beta-F-172 (◆), Sn-Beta-F-220 (●),Sn-Beta-OH-80 (○), Sn-Beta-OH-84 (△), and Sn-Beta-OH-94 (◇) after liquid water exposure for various durations (0-24 h, 373 K). The inset shows rate constants measured after short liquid water exposure times (0-1 h).

heterogeneities among the distribution of reactive environments within these samples, such as that provided by differences in the relative position of silanol groups to open Sn sites. This ~3x variation of first-order rate constants has also been observed on hydrophobic Ti-Beta-F and hydrophilic Ti-Beta-OH zeolites[36].

First-order rate constants (373 K, per open Sn) collected on Sn-Beta samples prior to hot water exposure were systematically higher by ~8x on Sn-Beta-F than on Sn-Beta-OH samples reported here (Table 2), similar to the differences (15–50x) in initial rates reported previously[22, 29]. Activation phenomena at short water exposure times and deactivation phenomena at long water exposure times were observed on each of the five Sn-Beta-F samples studied. In contrast, none of the three Sn-Beta-OH samples showed significant activation (>25% increase) at short water exposure times (Table 2), and all samples showed minimal deactivation (>25% decrease) after 24 h of water exposure at 373 K, reflected in rate constants that were similar regardless of water exposure time (Figure 1B).

These findings indicate that activation and deactivation upon water exposure (373 K) prior to reaction are general phenomena characteristic of Sn-Beta-F samples, but not Sn-Beta-OH samples. The extent of activation (χ_{act}), defined as the ratio of the highest isomerization rate constant measured after water exposure (typically 0.08–0.5 h at 373 K) to that on the untreated sample (Table 2), varied by 1.4-2.7x among the five Sn-Beta-F samples studied, indicating that the changes responsible for catalyst activation occur to different extents on each Sn-Beta-F sample. The increased turnover rates measured in the activation period on each sample are reproducible and outside of the experimental uncertainty for turnover rate measurements on a given sample (within 15%, not subject to sources of uncertainty from sample-to-sample variability responsible for 3x differences in rate constants between samples, details in Section S.2, Supp. Info). Sn-Beta-F samples deactivate and show similar isomerization rate constants (within ~1.5x) after 24 h of water exposure time. This deactivation behavior does not reflect the degradation of bulk crystalline structural properties,

Journal Name

ARTICLE

Table 2. First-order glucose-fructose isomerization rate constants (373 K) and extents of activation after exposure to hot (373 K) water exposure or NMe_4OH treatment.

Sample	First-Order Isomerization Rate Constant, 0 h Water Exposure (10^{-4} mol (mol glucose m^{-3})$^{-1}$ (mol open Sn)$^{-1}$ s^{-1})	Extent of Activation (χ_{act})	Water Exposure Time Corresponding to Maximum Rate (h)	First-Order Isomerization Rate Constant, 24 h Water Exposure (10^{-4} mol (mol glucose m^{-3})$^{-1}$ (mol open Sn)$^{-1}$ s^{-1})
Sn-Beta-F-100	1.24	2.7	0.083	0.27
Sn-Beta-F-172	1.21	2.1	0.083	0.25
Sn-Beta-F-220	1.16	1.8	0.17	0.32
Sn-Beta-F-116	1.74	2.0	0.17	0.41
Sn-Beta-F-110	3.93	1.4	0.17	0.42
Avg. Sn-Beta-F	*1.86*	*2.0*		*0.33*
Sn-Beta-OH-80	0.19	1.1	0.17	0.09
Sn-Beta-OH-94	0.48	1.1	0.083	n.m.*
Sn-Beta-OH-84	0.04	1.4	8.8	0.14
Avg. Sn-Beta-OH	*0.24*	*1.2*		*0.12*
Sn-Beta-F-100 (after NMe_4OH Treatment)	1.52	2.9		n.m.*

*n.m.: not measured.

evident in similar powder XRD patterns, micropore volume measurements, and SEM images before and after water exposure at 373 K (Figures S.8-S.10, Supp. Info.).

The preservation of long-range crystalline structure after water treatment times corresponding to activation and deactivation phenomena suggests that hot (373 K) water exposure influences the local structure of active Sn sites or of their surrounding microporous environments in the case of Sn-Beta-F, but not in the case of Sn-Beta-OH. Dissociative adsorption of water at closed Sn sites (Sn-$(OSi)_4$) facilitates interconversion of framework Sn between hydrolyzed-open ((HO)-Sn$(OSi)_3$ + Si-OH) and closed configurations as detected experimentally by ^{119}Sn NMR spectra through changes in Sn coordination from tetrahedral (-420 to -440 ppm) to octahedral (-690 to -720 ppm) upon water adsorption and hydrolysis of Sn-O-Si linkages[31, 33], and computationally using density functional theory (DFT) calculations (BEEF-vdW) of water dissociation reactions at closed Sn sites that access both open and closed configurations via quasi-equilibrated steps during ethanol dehydration catalysis (404 K, 0.1–50 kPa H_2O)[45, 46]. Such changes to Sn structure in the presence of water would influence measured rate constants, given that open Sn sites are dominant active sites for glucose-fructose isomerization[21-23]. Dissociative adsorption of water has also been reported to facilitate cleavage of framework siloxane bonds to form silanol defects in neutral or basic solutions[14, 47], which could also influence measured rate constants given that hydrophilic confining environments increase apparent activation Gibbs free energies compared to their hydrophobic analogs (Sn-Beta[22], Ti-Beta[27, 36]). Given that the number and coordination of framework Lewis acidic Sn sites and residual silanol defects are two structural features that influence glucose-fructose isomerization rate constants in Sn-Beta, we next probe changes in these two properties of Sn-Beta zeolites in response to hot liquid water exposure to determine more precisely the mechanisms underlying the activation and deactivation phenomena observed on Sn-Beta-F samples.

3.2. Characterization of Sn Sites in Sn-Beta as a Function of Water Exposure

The evolution of the number and structure of Sn sites was studied by exposing Sn-Beta-F-116, a representative Sn-Beta-F sample, to hot water (373 K) for various times followed by characterization of the bulk structure and surface sites on the recovered solids. The bulk Sn content determined from elemental analysis does not vary systematically with water exposure time and is identical (within error) after 24 h of hot water exposure (Figure S.11A, Supp. Info.). This indicates that

Sn leaching from the framework into solution is negligible, which is consistent with prior elemental analysis characterization using energy-dispersive X-ray analysis (SEM-EDX) of Sn-Beta after 150 h of continuous aqueous-flow exposure (413 K)[19], and inductively coupled plasma optical emission spectroscopy (ICP-OES) of Sn-Beta after 50 h of continuous aqueous-flow exposure (373 K)[8, 37, 48].

The potential hydrolysis of framework Sn species to form extraframework SnO_x domains, which are essentially unreactive for glucose isomerization catalysis in acidic (pH = 4) aqueous solution[26], was probed by measuring IR spectra upon CD_3CN titration of water-treated Sn-Beta-F-116. Adsorption of CD_3CN onto Sn-Beta zeolites results in IR spectra similar to those collected on untreated materials (Figure S.5, Supp. Info.) and contain ν(C≡N) peaks centered at 2316, 2308, 2287, and 2275 cm^{-1}. The ν(C≡N) stretching frequency centered at 2287 cm^{-1} has been assigned to CD_3CN bound to undercoordinated Sn sites located in surfaces of SnO_x domains[22, 42], and the ν(C≡N) stretching frequencies centered at 2316 and 2308 cm^{-1} have been assigned to CD_3CN bound to open and closed framework Lewis acid sites[23, 49]. The fractions of Sn present as Lewis acid sites, defined as the sum of open and closed Lewis acidic Sn sites (Sn_{LA}), and as sites located in surfaces of extraframework SnO_x domains (Sn_{EX}) on Sn-Beta-F-116 as a function of hot water (373 K) exposure time are shown in Figure S.11 (Supp. Info.). Neither Sn_{LA} nor Sn_{EX} varies outside of experimental error or in a systematic manner with increasing hot water exposure time. This observation suggests either that the distribution of Sn within framework locations and in extraframework SnO_x domains does not change significantly upon hot water exposure, or that it reverts to a common distribution upon exposure to vacuum (673 K) during the *ex situ* conditions of the IR measurements. The formation of Sn_{EX} domains upon hot water exposure was further investigated by estimating Sn edge energies determined from Tauc plots (Figure S.12, Supp. Info.) derived from UV-Vis spectra measured on dehydrated samples (523 K, Figure S.13, Supp. Info.) recovered after hot water treatment. Edge energies vary between 3.7 and 4.3 eV regardless of hot water exposure time (edge energies >4.1 eV indicate predominantly isolated framework Sn^{4+} [50]). On all samples, UV-Vis spectra show bands centered around 200-230 nm that do not vary in position with extended water exposure, yet new bands appear at higher wavelengths (340-500 nm) upon hot water exposure (373 K, >3 h), reflecting the formation of some Sn_{EX} domains. Such domains are expected to be small (<3 nm) as peaks for SnO_x phases were not observed in powder XRD patterns of samples after extended hot water exposure (Figure S.8, Supp. Info.).

As in the case of the total Lewis acidic Sn density on Sn-Beta-F-116, which does not change upon extended hot (373 K) water exposure, the relative density of open and closed Sn sites (per Sn_{LA}) also does not change systematically with increasing duration of water exposure (Figure S.14). This observation is consistent with structural changes in framework Sn coordination, which can occur upon water adsorption at ambient conditions[31] or *in situ* (404 K, 0.1-50 kPa H_2O, 0.5-35 kPa MeOH) upon hydrolysis of closed Sn sites to form open Sn sites[46, 51], and are reversible upon exposure to the vacuum treatments (823 K) prior to CD_3CN titration. Open and closed Sn site distributions are equilibrated in DFT-based microkinetic modeling simulations of gas-phase ethanol dehydration catalysis that include the free energy barriers for water dissociation reactions at closed Sn sites in Sn-Beta zeolites (404 K, 0.5–35 kPa C_2H_5OH, 0.1–50 kPa H_2O)[45, 46]. Therefore, it is likely that an equilibrated distribution of open and closed Sn sites on each Sn-Beta sample is formed *in situ*, and reverts to a distribution that is different for each Sn-Beta sample upon *ex situ* vacuum exposure.

The possibility that extraneous anionic ligands at Sn sites, which may interfere with CD_3CN adsorption at such sites and thus with Sn site quantification from IR spectra of Sn-Beta saturated with CD_3CN, was probed by characterizing residual fluoride anions that remain on Sn-Beta-F after the oxidative treatments used to remove organic structure directing agents that are present after hydrothermal synthesis[52]. Fluoride anions are preferentially located within double four membered ring building units, as observed on siliceous zeolites by ^{19}F MAS NMR (-38.5 ppm), and are covalently bonded to framework tetrahedral atoms[53]. Figure 2 shows solid-state ^{19}F NMR spectra (normalized by sample mass for comparison) collected on Sn-Beta-F-100 and Sn-Beta-F-220 prior to water exposure and after 0.5 h of water exposure at 373 K.

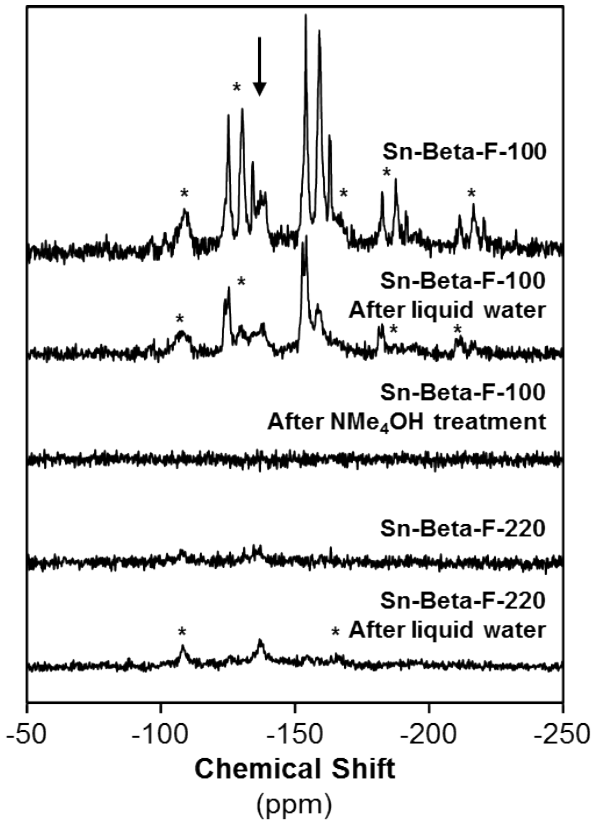

Figure 2. ^{19}F NMR spectra collected on Sn-Beta-F samples before liquid water exposure, after liquid water exposure, and after NMe_4OH treatment. The resonance centered at -135 ppm is marked with an arrow (* denotes spinning sidebands).

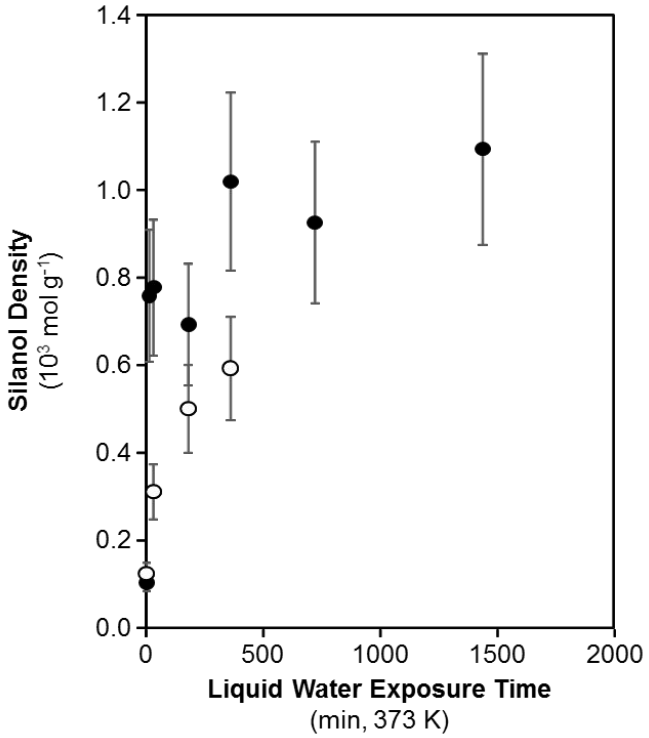

Figure 3. Silanol densities (per gram zeolite) on Sn-Beta-F-116 (●) and Sn-Beta-F-220 (○) as a function of liquid water exposure time.

A substantial amount of residual F is present in Sn-Beta-F-100, as indicated by resonances between -135 and -160 ppm and their spinning sidebands, which have previously been assigned to fluorine bound to hydrated and dehydrated Lewis acidic Sn sites, respectively[52]. A lower amount of residual F is present on Sn-Beta-F-220 despite the identical hydrofluoric acid content used in the hydrothermal synthesis of both Sn-Beta-F-220 and Sn-Beta-F-100. After exposure of Sn-Beta-F-100 to hot water for 0.5 h, ^{19}F resonances remain centered at identical chemical shifts (Figure 2) but decrease in intensity (by ~2x), reflecting partial defluorination of the solid. Open and closed Sn site densities (per Sn_{LA}) on Sn-Beta-F-100, however, did not change significantly after partial defluorination, suggesting that the presence of residual fluoride did not interfere with the quantification of Lewis acid sites using CD_3CN IR and that the presence of distinct IR peaks centered at 2316 cm^{-1} and 2308 cm^{-1} for CD_3CN-saturated Sn-Beta-F samples likely do not reflect any influence of F^- anions on framework Sn sites.

This hypothesis was tested further by treating Sn-Beta-F-100 with aqueous NMe_4OH, which has been previously observed to remove all occluded fluorine from hydrophobic Ti-Beta-F zeolites[54]. The NMR spectrum collected on Sn-Beta-F-100 after NMe_4OH treatment (Figure 2) shows no ^{19}F resonances, indicating removal of occluded fluorine without disruption of bulk crystalline properties or Sn site densities (additional details including XRD, UV-Vis, and CD_3CN IR in Section S.4, Supp. Info.). The extent of activation observed on Sn-Beta-F-100 after NMe_4OH treatment does not change upon F removal (Table 2), and a similar χ_{act} value (2.9x, Table 2) is measured on Sn-Beta-F-220 despite the residual presence of small amounts of F before and after water treatment. These findings indicate that the residual F content on a given Sn-Beta-F sample is not related to the activation phenomena observed upon hot (373 K) water treatment.

In summary, these data indicate that Sn site speciation is not significantly affected by hot (373 K) water exposure time. Open and closed Sn densities, and total Lewis acidic Sn densities, remain essentially constant with increasing water exposure time (0-24 h), although Sn_{EX} domains are observable in UV-Visible spectra and residual F^- anions are removed from the samples into solution. Collectively, this evidence does not suggest that there are significant changes in Sn speciation and location upon extended hot (373 K) water exposure. We next characterize changes in surface polarity as a function of extended hot water exposure by quantifying silanol defect densities.

3.3. Characterization of Silanol Densities in Sn-Beta as a Function of Water Exposure Duration

Figure 3 shows silanol defect densities quantified from gas-phase CD_3CN titration measured on Sn-Beta-F-116 and Sn-Beta-F-220 as a function of hot water exposure time. Silanol densities increase by ~2.5x and ~7.5x on Sn-Beta-F-220 and Sn-Beta-F-116 even after short water exposure times (0.08–0.5 h, Table 3), and continue to increase with longer durations of water exposure. These findings are consistent with qualitative

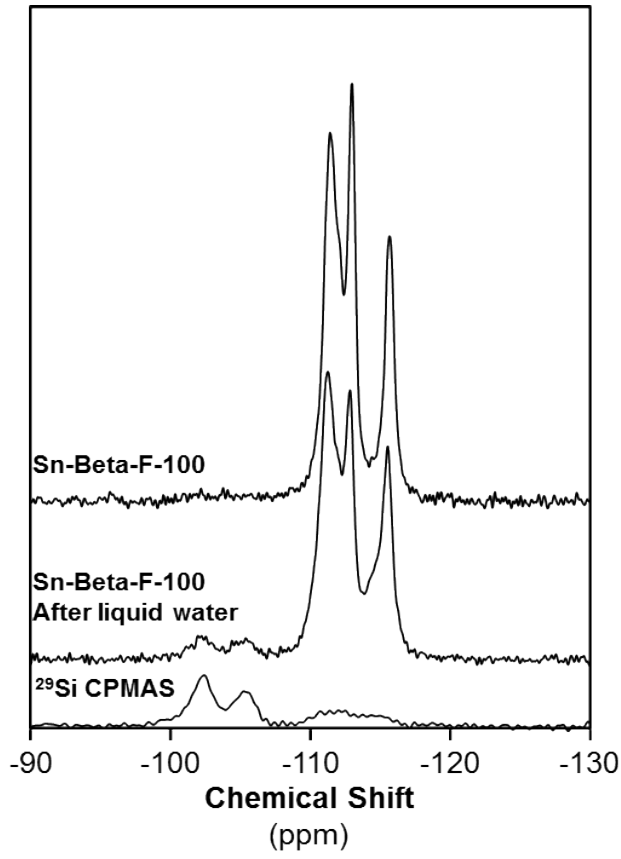

Figure 4. ^{29}Si MAS NMR spectra of Sn-Beta-F-100 before liquid water exposure and after 0.5 h of liquid water exposure, and ^{29}Si CPMAS NMR (contact time of 2 ms) after water exposure.

increases in silanol density that are reflected in higher areas for IR peaks centered at 3740 cm^{-1}, as previously observed on Sn-Beta zeolites after exposure to aqueous-phase glucose isomerization conditions (373 K) for 6 h[37]. Figure 4 shows ^{29}Si MAS and CPMAS NMR spectra of Sn-Beta-F-100 and ^{29}Si MAS and CPMAS NMR spectra of Sn-Beta-F-100 before and after 0.5 h of hot water exposure where the majority of the signal ranges between -109 and -119 ppm, representing Q^4 silicon sites whose assignments are consistent with ^{29}Si NMR resonances reported for pure silica Beta zeolites[55]. After water exposure, ^{29}Si MAS NMR shows a ~2.8x increase (relative to Q^4 Si resonance areas) in the areas of Q^3 Si resonances centered at -102.3 and -105.5 ppm for Si-OH groups, and their presence was further confirmed by ^{29}Si CPMAS NMR. We thus conclude that extended hot (373 K) water exposure leads to hydrolysis of siloxane linkages and increases the density of silanol defects on Sn-Beta-F samples.

The location of silanol defects within microporous environments can be characterized by vapor-phase methanol and water adsorption isotherms on Sn-Beta-F samples. Figure 5A shows methanol adsorption isotherms (293 K, P/P_0=0–0.6) on Sn-Beta-F-116 as a function of extended hot water exposure time. Methanol adsorption isotherms show Type V isotherm behavior on untreated Sn-Beta-F-116 and after short water exposure times (0–3 h), reflecting weak adsorbate-adsorbent interactions that dominate at low relative pressures (P/P_0=0–0.06) followed by adsorbate-adsorbate hydrogen-bonding interactions that drive microporous condensation at higher pressures (P/P_0=0.1–0.6). This adsorption behavior is consistent with previously reported methanol adsorption isotherms within hydrophobic Sn-Beta-F and Ti-Beta-F zeolites and reflects microporous environments comprising non-polar siloxane linkages incapable of hydrogen bonding with methanol molecules[22, 29, 44, 51]. As Sn-Beta-F-116 is exposed to hot water for longer times, vapor-phase methanol adsorption isotherms increasingly resemble Type I isotherms in shape, reflecting strong adsorbate-adsorbent interactions that lead to micropore filling. On average, adsorbate-adsorbent interactions gradually strengthen with increasing hot water exposure time, as evidenced by increased methanol uptakes at low relative pressures (P/P_0=0–0.06). Qualitatively, these isotherms gradually shift from Type V to Type I with increasing water treatment time, and concomitantly with a ~7.5x increase in silanol defect density. The Type I methanol isotherm behavior exhibited by samples exposed to extended hot water treatment (373 K, ≥12 h) reflects sufficient intraporous silanol densities to result in comparable methanol adsorption behavior to hydrophilic Sn-Beta-OH samples (Figure S.7, Supp. Info.).

Figure 5B shows vapor-phase water adsorption isotherms (293 K, P/P_0=0-0.6) on Sn-Beta-F-116 with varying hot water exposure time. Vapor-phase water adsorption isotherms on Sn-Beta-F-116 prior to hot water exposure are characteristic of hydrophobic Beta zeolites and follow a Type I isotherm, indicative of strong adsorbate-adsorbent interactions that result in water adsorption. These strong interactions reflect a combination of water adsorption onto Lewis acid sites and silanol groups. Water uptakes on Sn-Beta-F-116 (P/P_0=0–0.6) increase monotonically with increasing hot water exposure time and concomitantly with increasing silanol density (Figure

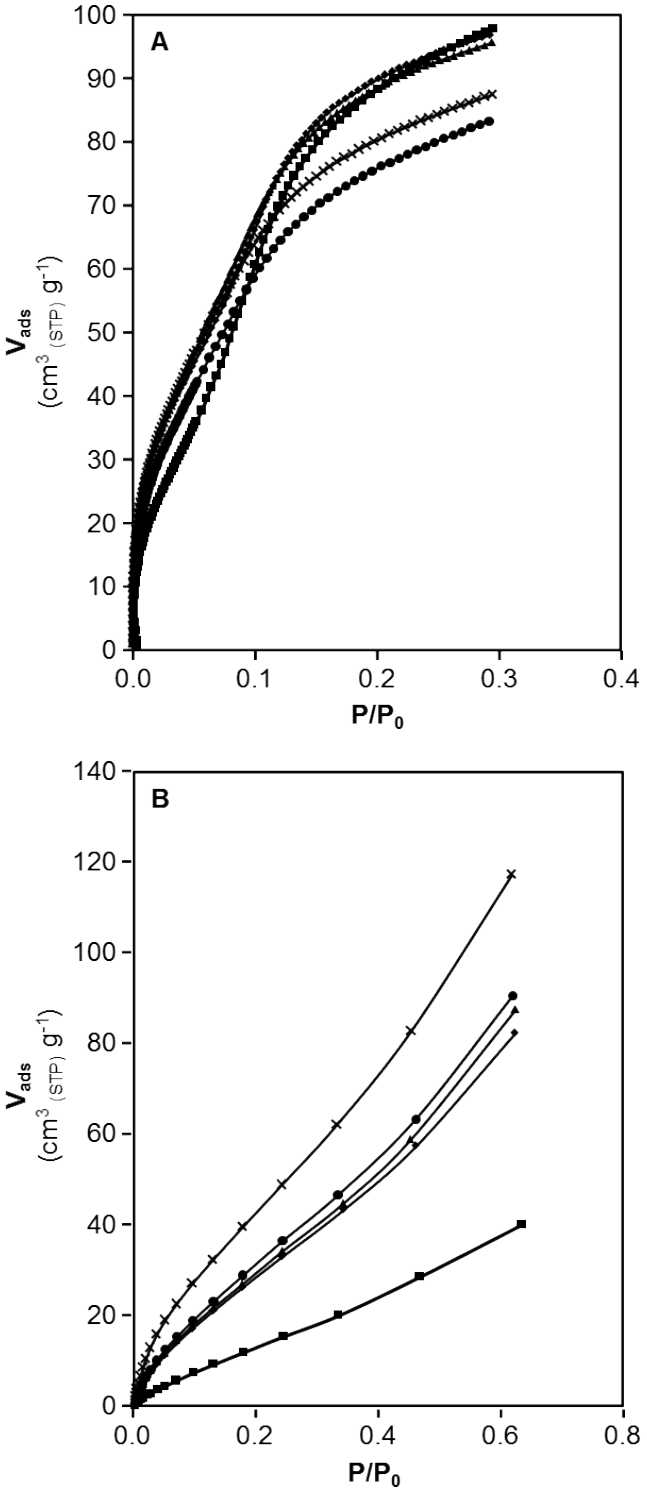

Figure 5. A) Vapor-phase methanol adsorption (293 K) isotherms collected on untreated Sn-Beta-F-116 (■) and on Sn-Beta-F-116 after 0.5 (◆), 3 (▲), 6 (X), and 24 (●) h of hot (373 K) liquid water exposure time. B) Vapor-phase water adsorption (293 K) isotherms collected on untreated Sn-Beta-F-116 (■) and on Sn-Beta-F-116 after 0.5 (◆), 3 (▲), 6 (X), and 24 (●) h of hot (373 K) liquid water exposure time.

S.17, Supp. Info.), as observed previously on Sn-Beta and Ti-Beta samples. These isotherms increasingly resemble water adsorption isotherms collected on Sn-Beta-OH samples (Figure S.6, Supp. Info.), indicating that the initially hydrophobic micropores of Sn-Beta-F have become substantially hydrophilic because of intraporous silanol formation. Having identified and quantified changes to both Lewis acidic site densities and intraporous defect density with increasing water exposure, we next discuss the observed deactivation of Sn-Beta catalysts for aqueous-phase glucose isomerization in the context of site and structural changes to the zeolite samples.

3.4. Origin of the Aqueous-Phase Deactivation Phenomena on Hydrophobic Sn-Beta.

Open Sn site densities remain unchanged upon exposure to hot water (Figure S.14, Supp. Info.), indicating that the observed deactivation cannot be ascribed to the loss of active sites. In contrast, intraporous silanol defects increase with water exposure time (Figure 3), and such sites can stabilize higher intraporous water densities (Section 3.3). Our prior work has shown that extended solvent structures present under reaction conditions result in lower initial glucose-fructose isomerization rates on hydrophilic Ti-Beta-OH zeolites relative to hydrophobic Ti-Beta-F zeolites[36]. Figure 6 shows first-order fructose formation rate constants (per open Sn) on Sn-Beta-F and Sn-Beta-OH samples, both prior to hot water exposure and after 24 h of hot water exposure (373 K). First-order isomerization rate constants measured on untreated Sn-Beta-F samples are ~8x higher than on Sn-Beta-OH samples, yet decrease after 24 h of hot water exposure to values identical to first-order rate constants measured on Sn-Beta-OH materials (within ~2x, per open Sn).

Hydrophobic Sn-Beta-F materials stabilize significantly lower water densities than hydrophilic Sn-Beta-OH materials (Figure S.6, Supp. Info.), yet the formation of intraporous silanol groups when Sn-Beta-F materials are exposed to hot liquid water (Figure 4) leads to increased intraporous water densities when equilibrated with vapor-phase water (Figure 5B) and, in turn, with liquid-phase water. Higher intraporous water densities and increased extents of hydrogen bonding in the co-adsorbed water network, which are measured *in situ* on Ti-Beta-OH relative to Ti-Beta-F using attenuated total reflectance IR (ATR-IR) and transmission IR spectroscopy[36], entropically destabilize the 1,2-hydride shift transition states to increase apparent free energy barriers and lower glucose isomerization rates in turn[36]. These findings, extended to Sn-Beta, are consistent with the higher rate constants measured on untreated hydrophobic Sn-Beta-F zeolites than hydrophilic Sn-Beta-OH zeolites (Figure 1), and with the formation of additional intraporous silanol defects leading to increased co-adsorbed water densities in Sn-Beta-F and concomitant increases to apparent free energy barriers after extended hot water exposure time (373 K, ~24 h), until co-adsorbed water densities are sufficient to fully occupy microporous reaction environments, as in the case of untreated Sn-Beta-OH. At this point, additional silanol groups do not lead to further changes in co-adsorbed water content nor, in turn, to apparent free energy barriers for glucose-fructose isomerization. Therefore, the deactivation of Sn-Beta-F after extended hot water exposure reflects the formation of intraporous silanol defects to stabilize extended water structures under aqueous-phase reaction conditions and increase apparent free energy barriers for glucose isomerization.

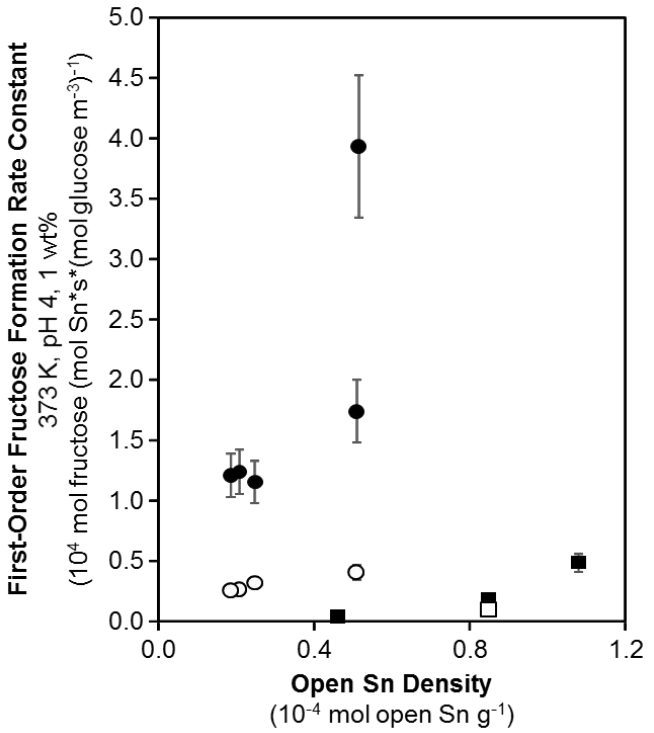

Figure 6. Measured first-order glucose isomerization rate constants on Sn-Beta-F samples prior to liquid water exposure (●), Sn-Beta-F samples after 24 h of liquid water exposure (○), Sn-Beta-OH samples prior to liquid water exposure (■), and Sn-Beta-OH samples after 24 h of liquid water exposure (□).

Other proposed deactivation mechanisms for Sn-Beta materials during aqueous-phase oxygenate conversion include Sn leaching from the zeolite framework and the coking or fouling of Lewis acid sites by product or byproduct formation[8, 37, 48]. Framework Sn leaching, the formation of Sn_{EX} species, and irreversible local structural changes to less reactive Sn species (i.e., closed Sn sites) are inconsistent with the data reported here using Sn elemental analysis and Lewis acid site densities quantified by CD_3CN titrations (Figures S.11 and S.14) measured as a function of hot (373 K) water exposure time. Product inhibition of active sites, which would hinder the ability for glucose to adsorb and isomerize, is also negligible under the conditions studied here, as the addition of small amounts of water (1–10 wt%, 383 K) during continuous flow minimizes the adsorption of other compounds of Sn sites during glucose isomerization in methanol[18, 56]. Product inhibition also cannot explain the decrease in initial rate measurements because products are absent at initial reaction times. Thus, the findings reported here reveal another mechanism of deactivation reflecting structural changes to intraporous reaction environments, in addition to prior reports indicating that solvent or product inhibition is a deactivation

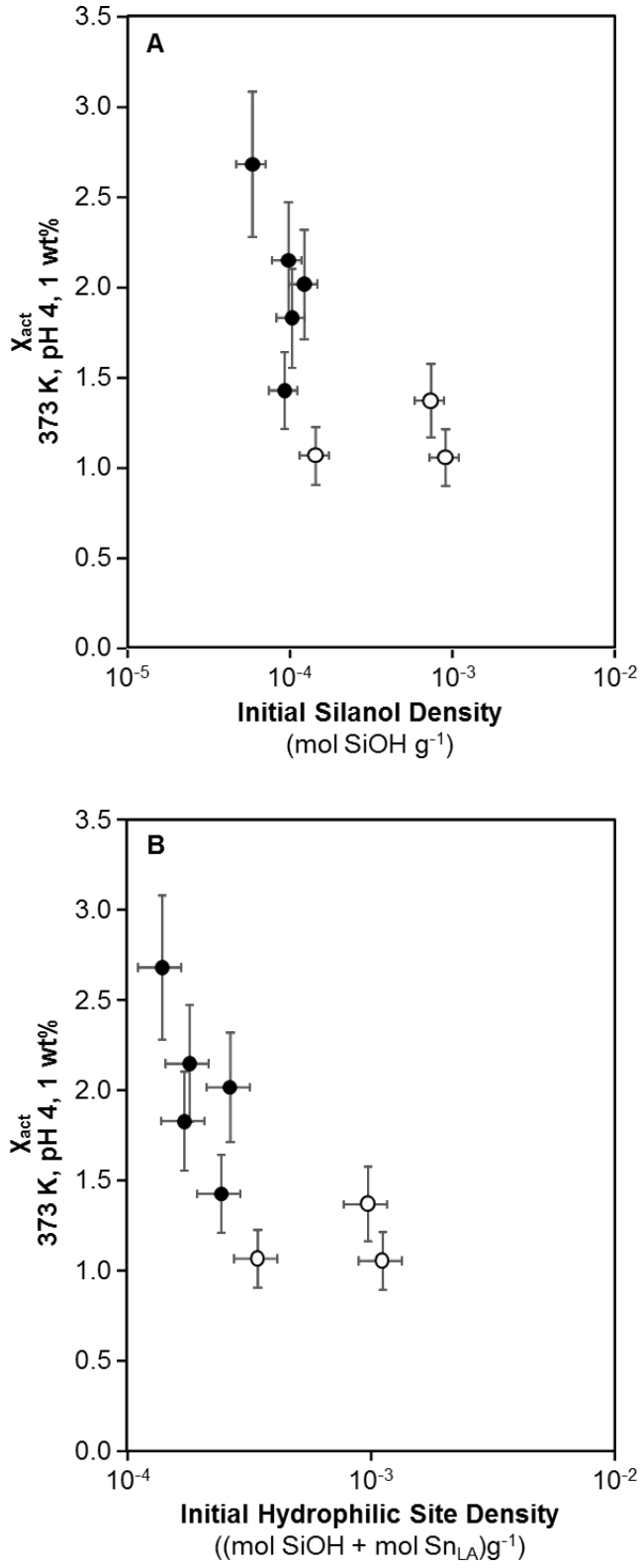

Figure 7. A) Observed activation extents (373 K, 1 wt%) as a function of initial silanol density on Sn-Beta-F (●) and Sn-Beta-OH (○) zeolites. B) Observed activation extents (373 K, 1 wt%) as a function of initial hydrophilic site density on Sn-Beta-F (●) and Sn-Beta-OH (○) zeolites. Hydrophilic sites represent the linear combination of silanol defects and Lewis acidic Sn centers on a given sample.

mechanism observed during glucose isomerization in water (373 K) at higher conversions (~20–50%) and in methanol at high temperatures (383-433 K)[37, 57]. We note that product inhibition may become more prominent at increased glucose concentrations that correspond to regimes in which glucose occupies larger fractions of microporous voids and become most abundant surface intermediates at active sites, in contrast to the conditions studied here that correspond to dilute glucose concentrations that lead to water as the most abundant surface intermediate.

We conclude that the deactivation observed here on Sn-Beta-F under aqueous-phase glucose isomerization conditions is attributed to the conversion of hydrophobic siloxane linkages into hydrophilic silanol defects within microporous voids. These intraporous silanol groups stabilize higher water densities within reactive environments and increase apparent free energy barriers for glucose-fructose isomerization. The formation of silanol defects as the primary aqueous-phase deactivation mechanism would be consistent with the irreversible nature of Sn-Beta deactivation observed previously, despite oxidative treatments (823 K) used to attempt to regenerate these catalysts[19], which may be insufficient to condense silanol pairs. We surmise that higher temperature oxidative treatments (>873 K) may be able to condense larger fractions of intraporous geminal silanol groups[58], potentially resulting in the recovery of more hydrophobic reaction environments and therefore higher initial isomerization rates. Next, we discuss the activation phenomena observed at short hot water exposure times (0-3 h) to rationalize the site and surface changes responsible for increased aqueous-phase glucose isomerization rates.

3.5. Speculations on the Origin of the Activation Phenomena on Hydrophobic Sn-Beta.

Figure 7A shows χ_{act} values measured on all Sn-Beta catalysts as a function of initial silanol density measured on the untreated samples. Values of χ_{act} appear to decrease systematically with increasing silanol density on Sn-Beta-F samples and are invariant with silanol density on Sn-Beta-OH materials. Further, activation phenomena are only observed on samples that initially contain low silanol densities (<2x10^{-4} mol silanol g^{-1}), after which higher silanol densities do not significantly impact measured χ_{act} values. This implies that there is a critical density of silanol groups and co-adsorbed water beyond which activation phenomena are not observed under the conditions studied here. We note that similar activation phenomena to that observed on Sn-Beta-F is also observed on hydrophobic Ti-Beta zeolites (Figure S.18, Supp. Info.), indicating that such activation is not dependent on heteroatom identity, and further suggesting that kinetic observations on Ti-Beta zeolites of varying defect density can be extended to Sn-Beta zeolites.

Water molecules within Ti-Beta zeolites have been reported to lower activation enthalpies by assisting in hydride transfer events[59], despite increasing activation entropies through the frustration of translational and rotational degrees of freedom. DFT-predicted apparent activation enthalpies and

entropies both increase systematically with increasing co-adsorbed water density[36]. Given that the exact influences of water on enthalpic barriers are unclear from these literature reports, we surmise that the presence of water molecules or clusters near Lewis acid sites, in a density higher than initially present within low-defect Sn-Beta-F zeolites, results in enthalpy-entropy compromises that lower apparent activation free energies for glucose-fructose isomerization that lead to higher initial measured rates. Further increases of additional intraporous water molecules cause increases to free energy barriers because of entropic destabilization of the 1,2-hydride shift transition state, eventually resulting in lower fructose formation rates[36].

Direct quantification of intraporous water content during reaction (per Sn_{LA}), and thus of the precise amount of water that minimizes free energy barriers and maximizes initial glucose isomerization rates, is convoluted by at least two factors. First, Lewis acidic Sn sites are capable of binding two water molecules that can stabilize small water clusters. The exact number of water molecules contained within second (or larger) solvation spheres through hydrogen-bonding networks will also depend on the proximity of other hydrophilic binding sites, such as silanol groups or framework Sn sites. Second, glucose adsorption into hydrophobic reaction environments entrains small quantities of water molecules from the solution-phase solvation sphere of glucose, as noted by increased water bending modes in *in situ* ATR-IR spectra at low glucose concentrations[36]. While these two factors cannot be quantitatively accounted for with current experimental techniques, Figure 7B shows χ_{act} values as a function of hydrophilic binding site density, which is defined as the sum of the silanol defect density and the Lewis acid site concentration on the untreated Sn-Beta material. Values of χ_{act} decrease systematically with increasing hydrophilic binding site density until approaching values near unity. Differences in the initial density of silanol groups, and their proximity to Sn_{LA} sites, may result in the ~3x variation in initial isomerization rates on untreated Sn-Beta samples (Figure 1B), via differences in co-adsorbed water densities proximal to Sn_{LA} sites that become irrelevant as microporous voids are filled with water. These findings are consistent with continuous-flow glucose isomerization rates in methanol that increase and then deactivate more slowly when small concentrations of water are added to the reaction mixture[18].

We note that χ_{act} values also correlate with *ex-situ* open Sn density, closed Sn density, open-to-closed ratio, Lewis acid site density, and even with the density of Sn_{EX} domains (per Sn, Figures S.19-S.23, Supp. Info.). The correlation with Sn_{EX} density is notable because Sn_{EX} species catalyze glucose-fructose isomerization through a base-catalyzed enolate intermediate[26]; however, these domains are inactive under the conditions studied here, evident from isotopic tracer studies using glucose-D2 reactants that show formation of only fructose-D_1 products (Figure S.24, Supp. Info.)[45, 46]. Therefore, the activation and deactivation phenomena evident in the turnover rate changes caused by hot water exposure, and the free energy differences they reflect, are most likely caused by differences in intraporous water content during catalysis.

Conclusions

The densities of hydrophilic surface groups and co-adsorbed water within microporous reaction environments influence catalytic turnover rates in aqueous media. The evolution in the number density of surface species, including framework Sn sites, extraframework Sn domains, and silanol defect groups, upon extended exposure to hot liquid water (373 K) were quantified using *ex situ* characterization techniques on Sn-Beta materials. Silanol concentrations increased with increasing duration (0-24 h) of hot water exposure, leading to concomitant changes in vapor-phase water uptakes (293 K) and a transition in vapor-phase methanol adsorption behavior (293 K) from Type V to Type I isotherms, indicating that the silanol groups formed from exposure to hot water are located within microporous reaction environments and can stabilize extended water networks during relevant aqueous-phase reaction conditions.

The catalytic implications of increased intraporous silanol densities and the co-adsorbed water structures they stabilize were probed using aqueous-phase glucose-fructose isomerization on hydrophobic Sn-Beta-F samples, which undergo activation (0-1 h) and eventual deactivation (>3 h) upon extended hot (373 K) water exposure. These activation and deactivation phenomena on Sn-Beta-F zeolites correlated with silanol densities, with low water densities appearing to enthalpically stabilize kinetically-relevant hydride shift transition states and higher water densities forming hydrogen-bonded networks that entropically destabilize hydride shift transition states via crowding effects, consistent with previous reports on Ti-Beta zeolites[36]. Enthalpic stabilization of sugar isomerization transition states by molecular water appears reminiscent of the reaction mechanism that occurs on the D-xylose isomerase enzyme[5], which contains an active site pocket that expels bulk water structures from the reaction environment while retaining molecular water to assist in proton shuttling events for glucose ring-opening and hydride transfer steps[5, 14].

These findings provide guidance for catalyst design strategies to attenuate deactivation of Sn-Beta-F in liquid water by mitigating the formation of intraporous silanol defects. One strategy involves tailoring the solvent mixture to maintain high isomerization rates[60-63], while mitigating intraporous silanol formation under reaction conditions, as in the case of methanol and water mixtures that maintain hydroxyl ligands on open Sn sites under glucose isomerization reaction conditions and minimize Sn-Beta deactivation[56]. A second strategy involves the modification of external crystallite surfaces using hydrophobic organosilanes, which hinders water diffusion into MFI micropores[64] and results in significant improvements Beta zeolite stability in hot water[11, 14, 16]. Overall, this study shows how combining quantitative *ex situ* characterization techniques and catalytic probe reactions, on a suite of zeolite samples containing Lewis acid active sites

confined within hydrophobic or hydrophilic environments, can be used to understand the structural changes underlying the deactivation of Lewis acid zeolites in liquid water.

Conflicts of interest

There are no conflicts to declare.

Acknowledgements

We acknowledge the financial support provided by the Purdue Process Safety and Assurance Center (P2SAC). We also thank Juan Carlos Vega-Vila for helpful technical discussions and comments on this manuscript. The NMR facility at the California Institute of Technology was supported by the National Science Foundation (NSF) under Grant Number 9724240 and partially supported by the MRSEC Program of the NSF under Award Number DMR-520565.

Notes and references

1. N. E. Thornburg, A. B. Thompson and J. M. Notestein, *ACS Catalysis*, 2015, **5**, 5077-5088.
2. M. G. Clerici, G. Bellussi and U. Romano, *Journal of Catalysis*, 1991, **129**, 159-167.
3. M. E. Davis, *Topics in Catalysis*, 2015, **58**, 405-409.
4. R. Gounder, *Catal. Sci. Technol.*, 2014, **4**, 2877-2886.
5. A. Y. Kovalevsky, L. Hanson, S. Z. Fisher, M. Mustyakimov, S. A. Mason, V. T. Forsyth, M. P. Blakeley, D. A. Keen, T. Wagner, H. L. Carrell, A. K. Katz, J. P. Glusker and P. Langan, *Structure*, 2010, **18**, 688-699.
6. S. H. Bhosale, M. B. Rao and V. V. Deshpande, *Microbiological Reviews*, 1996, **60**, 280-300.
7. J. D. Lewis, S. Van de Vyver, A. J. Crisci, W. R. Gunther, V. K. Michaelis, R. G. Griffin and Y. Roman-Leshkov, *ChemSusChem*, 2014, **7**, 2255-2265.
8. G. M. Lari, P. Y. Dapsens, D. Scholz, S. Mitchell, C. Mondelli and J. Perez-Ramirez, *Green Chemistry*, 2016, **18**, 1249-1260.
9. H. J. Cho, P. Dornath and W. Fan, *ACS Catalysis*, 2014, **4**, 2029-2037.
10. A. Vjunov, M. A. Derewinski, J. L. Fulton, D. M. Camaioni and J. A. Lercher, *Journal of the American Chemical Society*, 2015, **137**, 10374-10382.
11. S. Prodinger, H. Shi, S. Eckstein, J. Z. Hu, M. V. Olarte, D. M. Camaioni, M. A. Derewinski and J. A. Lercher, *Chemistry of Materials*, 2017, **29**, 7255-7262.
12. R. M. Ravenelle, F. Schussler, A. D'Amico, N. Danilina, J. A. van Bokhoven, J. A. Lercher, C. W. Jones and C. Sievers, *J. Phys. Chem. C*, 2010, **114**, 19582-19595.
13. N. Giovambattista, P. G. Debenedetti and P. J. Rossky, *J. Phys. Chem. C*, 2007, **111**, 1323-1332.
14. L. Zhang, K. Z. Chen, B. H. Chen, J. L. White and D. E. Resasco, *Journal of the American Chemical Society*, 2015, **137**, 11810-11819.
15. P. A. Zapata, Y. Huang, M. A. Gonzalez-Borja and D. E. Resasco, *Journal of Catalysis*, 2013, **308**, 82-97.
16. S. Prodinger, H. Shi, H. M. Wang, M. A. Derewinski and J. A. Lercher, *Applied Catalysis B-Environmental*, 2018, **237**, 996-1002.
17. P. A. Zapata, J. Faria, M. P. Ruiz, R. E. Jentoft and D. E. Resasco, *Journal of the American Chemical Society*, 2012, **134**, 8570-8578.
18. D. Padovan, S. Tolborg, L. Botti, E. Taarning, I. Sadaba and C. Hammond, *Reaction Chemistry & Engineering*, 2018, **3**, 155-163.
19. D. Padovan, C. Parsons, M. S. Grasina and C. Hammond, *Green Chemistry*, 2016, **18**, 5041-5049.
20. W. N. van der Graaff, C. H. Tempelman, G. Li, B. Mezari, N. Kosinov, E. A. Pidko and E. J. Hensen, *ChemSusChem*, 2016, **9**, 3145-3149.
21. R. Bermejo-Deval, R. S. Assary, E. Nikolla, M. Moliner, Y. Roman-Leshkov, S. J. Hwang, A. Palsdottir, D. Silverman, R. F. Lobo, L. A. Curtiss and M. E. Davis, *Proceedings of the National Academy of Sciences of the United States of America*, 2012, **109**, 9727-9732.
22. J. W. Harris, M. J. Cordon, J. R. Di Iorio, J. C. Vega-Vila, F. H. Ribeiro and R. Gounder, *Journal of Catalysis*, 2016, **335**, 141-154.
23. R. Bermejo-Deval, M. Orazov, R. Gounder, S. J. Hwang and M. E. Davis, *ACS Catalysis*, 2014, **4**, 2288-2297.
24. Y. Roman-Leshkov, M. Moliner, J. A. Labinger and M. E. Davis, *Angewandte Chemie-International Edition*, 2010, **49**, 8954-8957.
25. M. Moliner, Y. Roman-Leshkov and M. E. Davis, *Proceedings of the National Academy of Sciences of the United States of America*, 2010, **107**, 6164-6168.
26. R. Bermejo-Deval, R. Gounder and M. E. Davis, *ACS Catalysis*, 2012, **2**, 2705-2713.
27. R. Gounder and M. E. Davis, *Journal of Catalysis*, 2013, **308**, 176-188.
28. Y. P. Li, M. Head-Gordon and A. T. Bell, *ACS Catalysis*, 2014, **4**, 1537-1545.
29. J. C. Vega-Vila, J. W. Harris and R. Gounder, *J. Catal.*, 2016, **344**, 108-120.
30. N. K. Mal, V. Ramaswamy, P. R. Rajamohanan and A. V. Ramaswamy, *Microporous Materials*, 1997, **12**, 331-340.
31. A. V. Yakimov, Y. G. Kolyagin, S. Tolborg, P. N. R. Vennestrom and Ivanova, II, *J. Phys. Chem. C*, 2016, **120**, 28083-28092.
32. P. Wolf, M. Valla, A. J. Rossini, A. Comas-Vives, F. Nunez-Zarur, B. Malaman, A. Lesage, L. Emsley, C. Coperet and I. Hermans, *Angewandte Chemie-International Edition*, 2014, **53**, 10179-10183.
33. J. W. Harris, W. C. Liao, J. R. Di Iorio, A. M. Henry, T. C. Ong, A. Comas-Vives, C. Coperet and R. Gounder, *Chemistry of Materials*, 2017, **29**, 8824-8837.
34. S. R. Bare, S. D. Kelly, W. Sinkler, J. J. Low, F. S. Modica, S. Valencia, A. Corma and L. T. Nemeth, *Journal of the American Chemical Society*, 2005, **127**, 12924-12932.
35. J. Dijkmans, M. Dusselier, W. Janssens, M. Trekels, A. Vantomme, E. Breynaert, C. Kirschhock and B. F. Sels, *ACS Catalysis*, 2016, **6**, 31-46.
36. M. J. Cordon, J. W. Harris, J. C. Vega-Vila, J. S. Bates, S. Kaur, M. Gupta, M. E. Witzke, E. C. Wegener, J. T. Miller, D. W. Flaherty, D. D. Hibbitts and R. Gounder, *Journal of the American Chemical Society*, 2018, **140**, 14244-14266.
37. W. N. P. van der Graaff, C. H. L. Tempelman, F. C. Hendriks, J. Ruiz-Martinez, S. Bals, B. M. Weckhuysen, E.

A. Pidko and E. J. M. Hensen, *Applied Catalysis A: General*, 2018, **564**, 113-122.
38. C. C. Chang, Z. P. Wang, P. Dornath, H. J. Cho and W. Fan, *RSC Advances*, 2012, **2**, 10475-10477.
39. W. N. P. van der Graaff, G. Li, B. Mezari, E. A. Pidko and E. J. M. Hensen, *ChemCatChem*, 2015, **7**, 1152-1160.
40. N. Y. Chen, *Journal of Physical Chemistry*, 1976, **80**, 60-64.
41. V. J. Cybulskis, J. W. Harris, Y. Zvinevich, F. H. Ribeiro and R. Gounder, *Review of Scientific Instruments*, 2016, **87**, 8-15.
42. V. L. Sushkevich, I. I. Ivanova and A. V. Yakimov, *The Journal of Physical Chemistry C*, 2017, **121**, 11437-11447.
43. F. Gu, S. F. Wang, C. F. Song, M. K. Lu, Y. X. Qi, G. J. Zhou, D. Xu and D. R. Yuan, *Chem. Phys. Lett.*, 2003, **372**, 451-454.
44. R. Gounder and M. E. Davis, *AICHE Journal*, 2013, **59**, 3349-3358.
45. B. C. Bukowski and J. Greeley, *J. Phys. Chem. C*, 2016, **120**, 6714-6722.
46. B. C. Bukowski, J. S. Bates, R. Gounder and J. Greeley, *Journal of Catalysis*, 2018, **365**, 261-276.
47. P. Y. Dapsens, C. Mondelli, J. Jagielski, R. Hauert and J. Perez-Ramirez, *Catal. Sci. Technol.*, 2014, **4**, 2302-2311.
48. I. Sadaba, M. L. Granados, A. Riisager and E. Taarning, *Green Chemistry*, 2015, **17**, 4133-4145.
49. M. Boronat, P. Concepcion, A. Corma, M. Renz and S. Valencia, *Journal of Catalysis*, 2005, **234**, 111-118.
50. S. Roy, K. Bakhmutsky, E. Mahmoud, R. F. Lobo and R. J. Gorte, *Acs Catalysis*, 2013, **3**, 573-580.
51. J. S. Bates and R. Gounder, *Journal of Catalysis*, 2018, **365**, 213-226.
52. S. J. Hwang, R. Gounder, Y. Bhawe, M. Orazov, R. Bermejo-Deval and M. E. Davis, *Topics in Catalysis*, 2015, **58**, 435-440.
53. M. A. Camblor, P. A. Barrett, M. J. Diaz-Cabanas, L. A. Villaescusa, M. Puche, T. Boix, E. Perez and H. Koller, *Microporous and Mesoporous Materials*, 2001, **48**, 11-22.
54. Y. Goa, P. Wu and T. Tatsumi, *Journal of Physical Chemistry B*, 2004, **108**, 4242-4244.
55. M. A. Camblor, A. Corma and S. Valencia, *Chemical Communications*, 1996, 2365-2366.
56. D. Padovan, L. Botti and C. Hammond, *ACS Catalysis*, 2018, **8**, 7131-7140.
57. L. Botti, R. Navar, S. Tolborg, J. S. Martinez-Espin, D. Padovan, E. Taarning and C. Hammond, *Topics in Catalysis*, 2018.
58. A. M. Love, C. A. Carrero, A. Chieregato, J. T. Grant, S. Conrad, R. Verel and I. Hermans, *Chemistry of Materials*, 2016, **28**, 5495-5504.
59. G. N. Li, E. A. Pidko and E. J. M. Hensen, *Catal. Sci. Technol.*, 2014, **4**, 2241-2250.
60. M. H. Tucker, R. Alamillo, A. J. Crisci, G. M. Gonzalez, S. L. Scott and J. A. Dumesic, *ACS Sustainable Chemistry & Engineering*, 2013, **1**, 554-560.
61. M. A. Mellmer, C. Sener, J. M. R. Gallo, J. S. Luterbacher, D. M. Alonso and J. A. Dumesic, *Angewandte Chemie-International Edition*, 2014, **53**, 11872-11875.
62. L. Qi, R. Alamillo, W. A. Elliott, A. Andersen, D. W. Hoyt, E. D. Walter, K. S. Han, N. M. Washton, R. M. Rioux, J. A. Dumesic and S. L. Scott, *ACS Catalysis*, 2017, **7**, 3489-3500.
63. M. A. Mellmer, C. Sanpitakseree, B. Demir, P. Bai, K. W. Ma, M. Neurock and J. A. Dumesic, *Nature Catalysis*, 2018, **1**, 199-207.
64. K. Z. Chen, J. Kelsey, J. L. White, L. Zhang and D. Resasco, *ACS Catalysis*, 2015, **5**, 7480-7487.

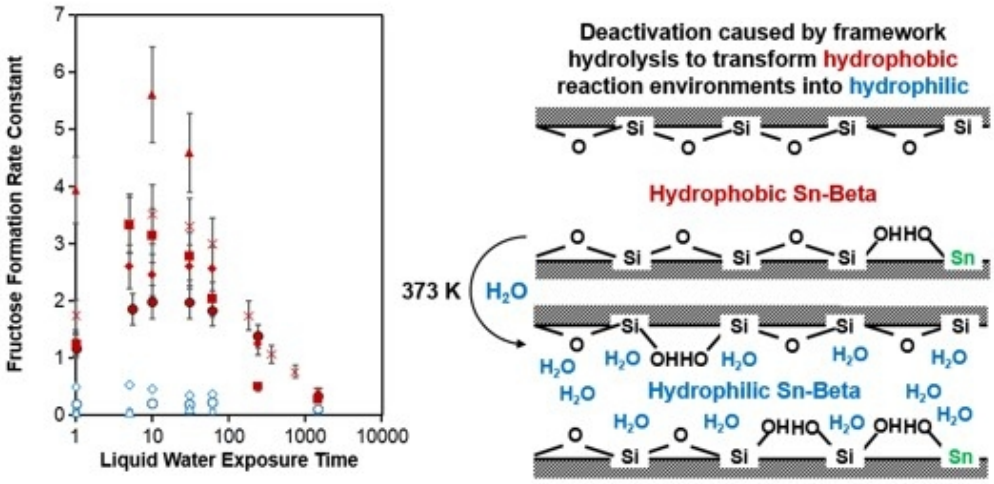

88x45mm (150 x 150 DPI)